Bimodal Crystallization at Polymer-Fullerene Interfaces

Dyfrig Môn[a], Anthony M. Higgins*[,a], David James[a], Mark Hampton[b], J. Emyr Macdonald[b], Michael B. Ward[c], Philipp Gutfreund[d], Samuele Lilliu[e], Jonathan Rawle[f]

[a] College of Engineering, Swansea University, Singleton Park, Swansea, SA2 8PP, United Kingdom
[b] School of Physics and Astronomy, Cardiff University, The Parade, Cardiff CF24 3AA, United Kingdom
[c] Institute for Materials Research, School of Process, Environmental and Materials Engineering, University of Leeds, Leeds, LS2 9JT, United Kingdom
[d] Institut Laue-Langevin, 71 avenue des Martyrs, 38000 Grenoble, France
[e] Nano-Optics and Optoelectronics Research Laboratory, Masdar Institute of Science and Technology, Block 3, Masdar City, PO Box 54224, Abu Dhabi, United Arab Emirates
[f] Diamond Light Source, Harwell Science and Innovation Campus, Didcot, Oxfordshire OX11 0DE, United Kingdom

*** Corresponding author** a.m.higgins@swansea.ac.uk

Supplementary Information

1. Supporting Experimental Data.

1.1 Temperature Dependence of Crystal Growth; Optical Microscopy.

Our main focus in this study was the comparison between isothermal growth of needles in various PS bilayers at 170 °C. However, some measurements were performed at other temperatures in order to i) control the needle-growth process and optimize the conditions for experimental measurements over a convenient timeframe, and ii) gain some further understanding of the PCBM crystal growth mechanisms. In pure PCBM the reported bulk T_g is 131 °C,[1] while the temperature above which cold-crystallization is observed in GIXD measurements is 142 °C in ~ 20-25nm PCBM films.[2] We used annealing-temperatures between 130 °C and 200 °C (well-above the T_g of bulk PS[3] and P3HT[1]) and found that both the nucleation-density and growth-rate of needle-like PCBM crystals changes substantially over this temperature range. Figs S1 and S2 show optical microscopy images of needle-like PCBM crystals in PS and P3HT bilayers, along with nucleation-density and crystal-size data for *ex-situ* annealed samples. In both systems the mean length of the observed crystals after two hours annealing, increases significantly with annealing-temperature, while the density of nucleated crystals reduces with annealing-temperature. The combination of these two factors is responsible for the tentative evidence of a maximum in the fractional area coverage of PCBM crystals with annealing-temperature, which occurs at a slightly higher temperature for PS bilayers compared to P3HT bilayers.

The reducing nucleation-density with temperature is likely to be because the energetic gain on crystallization, per PCBM molecule, reduces as the degree-of-undercooling below the PCBM melting temperature reduces, and hence (less-probable) larger-sized crystalline nuclei are required to overcome the energetic penalty due to the crystal/amorphous interface. *A priori* one might anticipate that the increased crystal-length with temperature is due to an increased PCBM molecular-mobility at higher temperature. We examined this further by comparing growth-curves of individual crystals at two different annealing-temperatures. Fig. S3 shows that similar shapes of growth-curves are found at 170 °C and 180 °C, with a growth-rate gradually diminishing from a maximum to zero. Raising the temperature by 10 °C (for a given film-thickness and MW) produces a significant increase in the early-time growth-rate of the needles (suggesting a reduced viscosity of the amorphous PCBM film), but also a faster approach to zero growth-rate (suggesting a faster nanocrystal growth). Fitting the 180 °C curves in fig. S3 using equation (1) with n, ϕ_m and m fixed at the parameter values obtained from the global fit at 170 °C (see fig. S19) we obtain K parameters of 0.0072 and 0.0082, and A parameters of 5.4 and 4.6 for the earlier and later nucleated crystals respectively at 180 °C. This represents a mean increase in A by a factor of ~2.4 and a mean increase in K by a factor of ~1.5 between 170 °C and 180 °C for 35nm 106k PS bilayer crystals (*cf* fig. S19b-c). We don't have information regarding the thermodynamics (eg the latent heat of fusion) governing the rate at which amorphous PCBM molecules join the growing micron-sized crystal front in the presence of PS. However the degree-of-undercooling, and hence free energy gain on crystallization will *reduce* by about 10% between 170 °C and 180 °C,[4] tending to cause the crystallization rate to either reduce or remain unchanged (depending on the value of latent heat of fusion). This leads us to conclude that the *increased* A and K parameters at 180 °C are indeed most likely due to increases in the PCBM molecular-mobility with temperature.

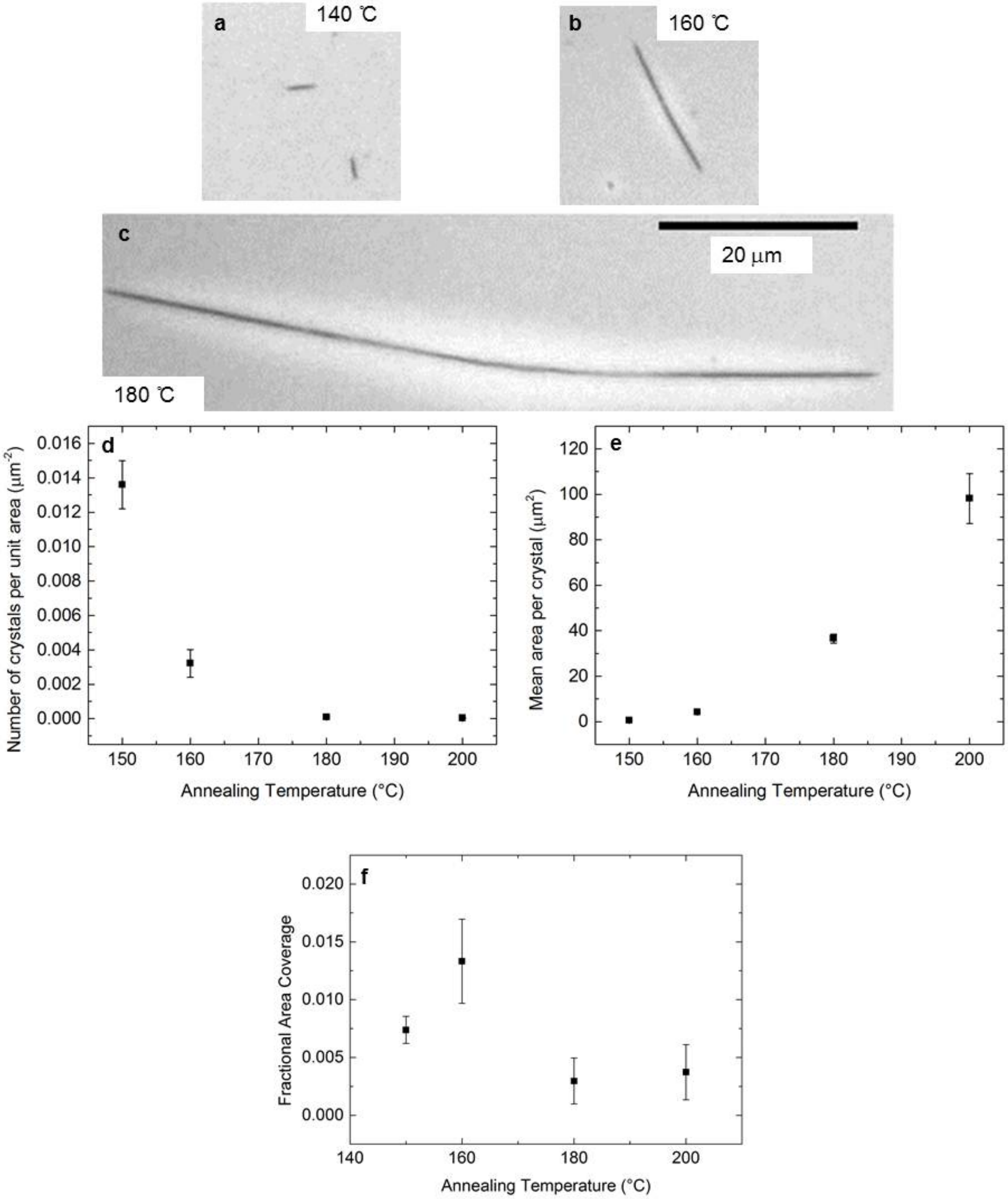

Figure S1. (a)-(c) Optical micrographs of Silicon/PCBM(20nm)/344k-PS(40nm) bilayers *ex-situ* annealed at various temperatures for 2 hours. The scale bar is common to all 3 images. (d) Density of needle-like crystals after 2 hours annealing as a function of temperature. (e) Crystal size as a function of annealing temperature. (f) Fractional area covered by crystals (the product of (d) and (e)) as a function of annealing temperature. These measurements were done on a single batch of samples, with the silicon substrates used as-received.

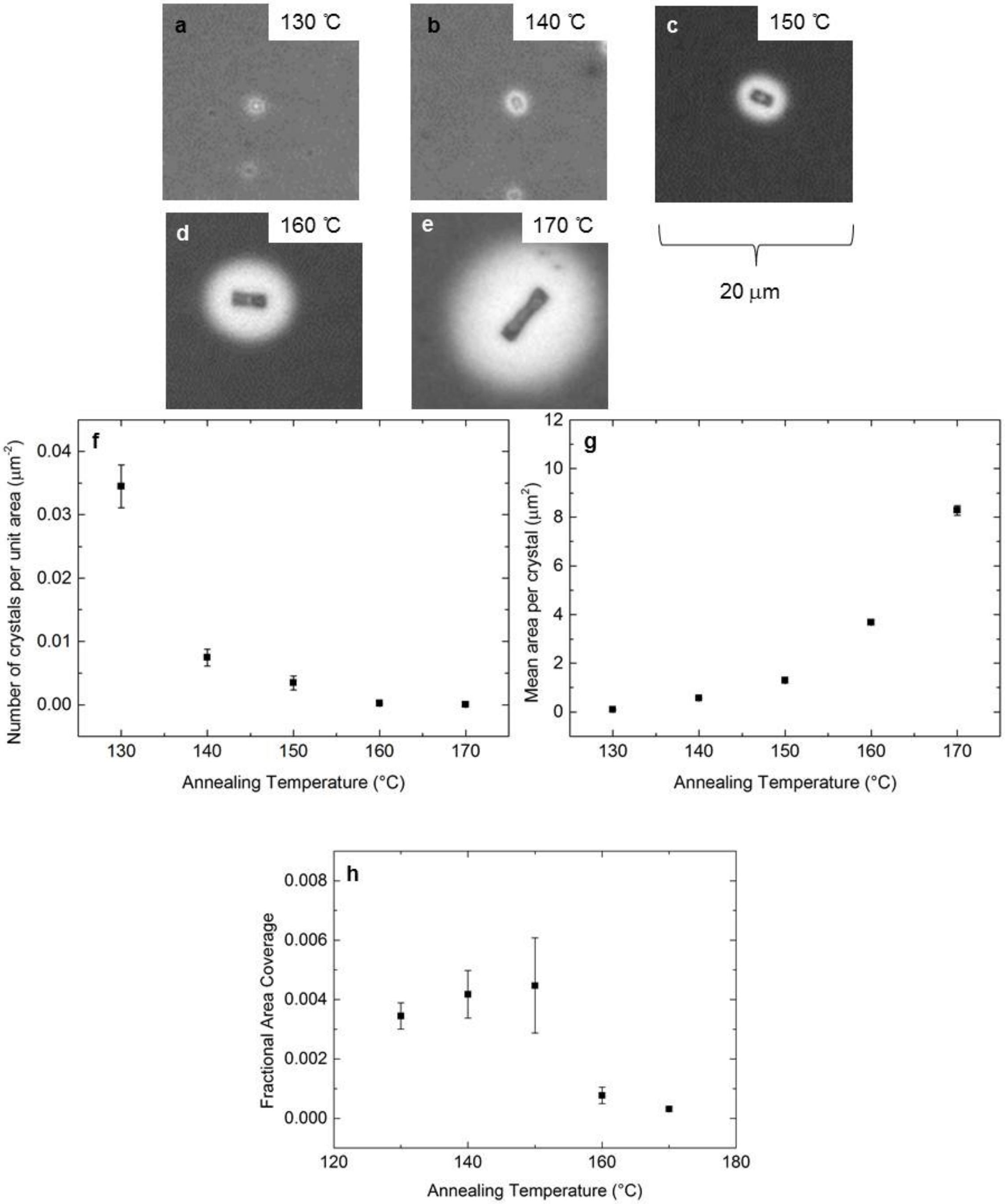

Figure S2. (a)-(e) Optical micrographs of Silicon/PCBM(20nm)/P3HT(25nm) bilayers *ex-situ* annealed at various temperatures for 2 hours. All images are 20μm x 20μm. (f) Density of needle-like crystals after 2 hours annealing as a function of temperature. (g) Crystal size as a function of annealing temperature. (h) Fractional area covered by crystals (the product of (f) and (g)) as a function of annealing temperature. These measurements were done on a single batch of samples, with the silicon substrates used as-received.

We note that there is some variability in the nucleation density of needle-like crystals within and between some (nominally duplicate) samples, particularly those prepared using the sonication/rinsing protocol. However, from *in-situ* measurements we find that the crystal growth-rates are unaffected by the nucleation density.

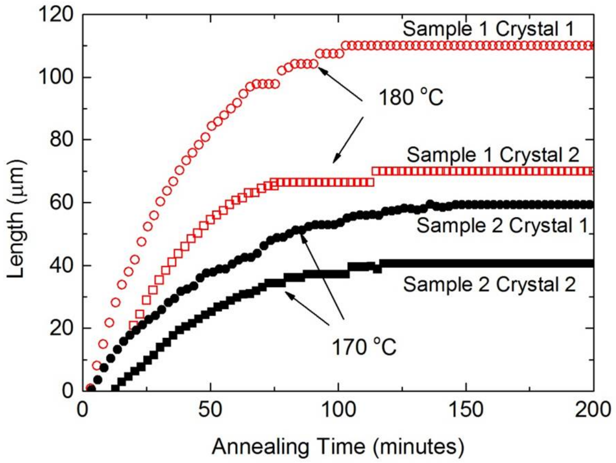

Figure S3. *In-situ* optical microscopy growth-curves for needle-like PCBM crystals in two different 35nm 106k-PS bilayer samples annealed at 170 °C and 180 °C. This data was obtained using a mercury-lamp illumination source.

1.2 Geometry of Growing Needle Tips; AFM and Optical Microscopy.

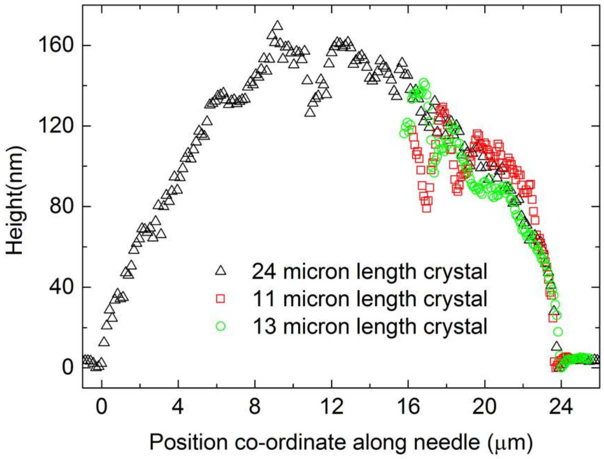

Figure S4. AFM profiles of individual crystals on a single PCBM/344k-PS(25nm) bilayer sample annealed at 170 °C for 24 minutes.

Fig. S4 shows AFM height-profiles along the main axis of a selection of different needles on a single sample and fig. S5 shows a selection of AFM height-profiles near the tips of a selection of different crystals on various samples. Fig. S6 shows needle-widths measured by AFM for a selection of crystals and fig. S7 shows three optical microscopy snapshots of the tips of three individual crystals during *in-situ* annealing. The needle-profiles and needle-widths show some sample-sample and crystal-crystal (within a single sample) variation, but show little clear systematic dependence on PS-thickness, molecular-weight or annealing-times over and above the observed sample-sample and crystal-crystal variability (fig. S6 shows some PS thickness dependence of the crystal width, but all within a range of approximately 0.7 to 2μm). The crystal profiles measured in this study exhibited very similar growth-rates in the two opposite growth directions (i.e. in both directions from the location of the crystal nucleus, pointing along the main crystal axis at 180° to one another). This bidirectional symmetry and the symmetric height-profile of the crystals (see fig. S4) suggests that the needles are well oriented with respect to the substrate/polymer interface, with a fast-growing crystal-plane perpendicular to the substrate-normal. We also note the observation, by *in-situ* optical microscopy, of some crystals that nucleate but do not grow into needles, and also of short (<5μm length) needle-like crystals that only grow in one direction from the crystal nucleus. We did not include these types of crystal in the data-sets used for growth-curve fitting.

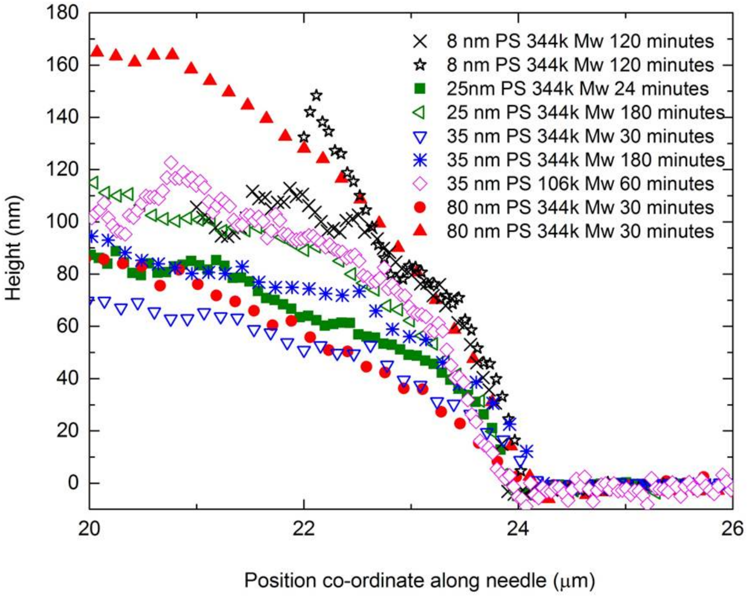

Figure S5. AFM profiles of individual crystals on PCBM/PS bilayers annealed at 170 ^{o}C for various times.

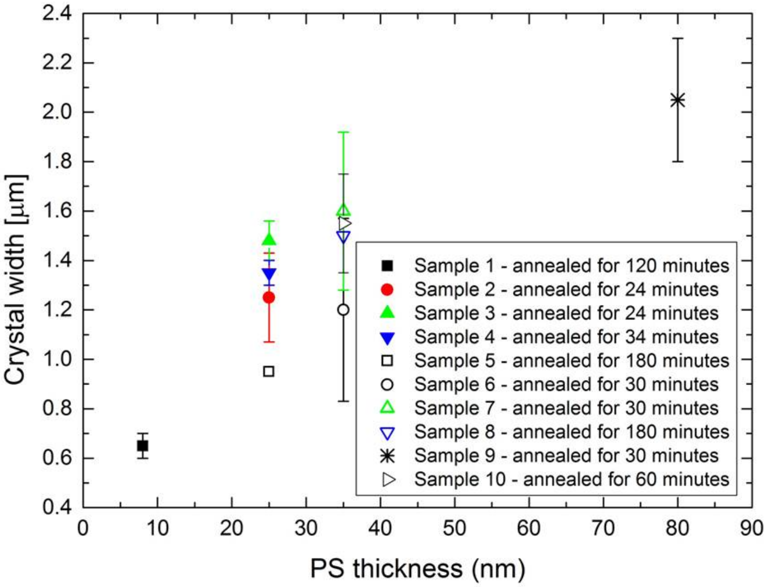

Figure S6. Average PCBM needle-like crystal widths as a function of PS-thickness for 10 different samples annealed at 170 ^{o}C for various times (measured as the full-width from the minimum in the trough on one side of the crystal to the minimum on the other side, at the half way point along the long crystal axis). Samples 1 to 9 used PS with a M_w of 344k. Sample 10 used PS with a M_w of 106k.

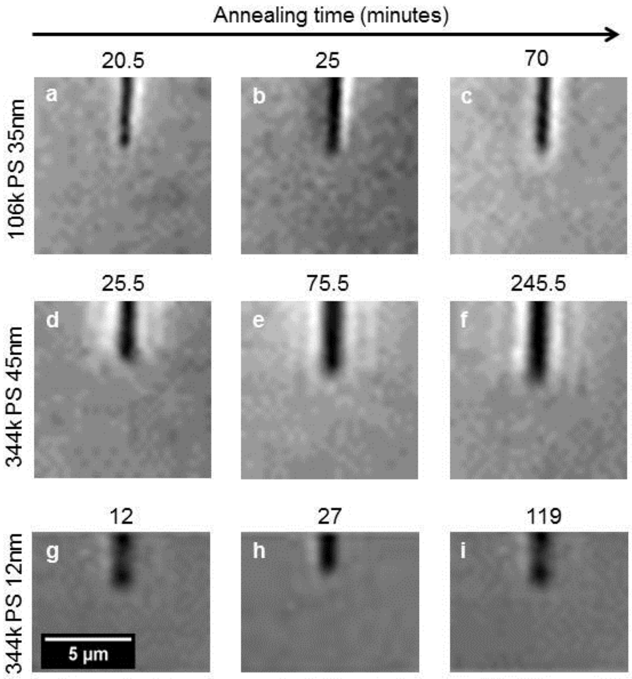

Figure S7. Snapshots from *in-situ* optical microscopy of individual growing crystal tips as a function of annealing time at 170 ^{o}C. All images are the same scale.

1.3 Polarized Optical Microscopy of Needles.

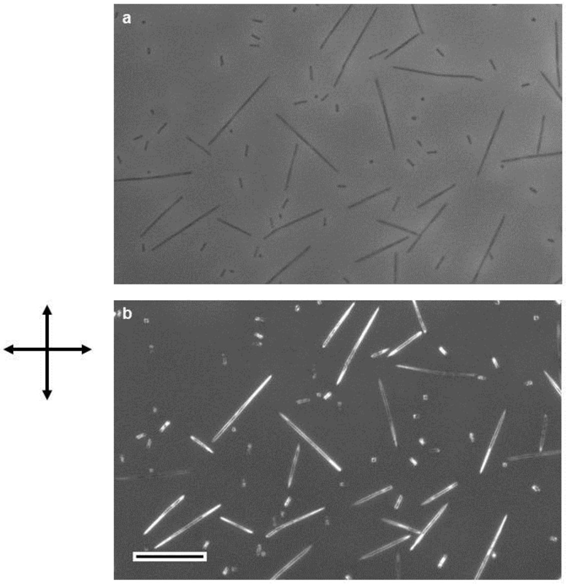

Figure S8. Optical micrographs of the same area of a PCBM(20nm)/344k-PS(25nm) bilayer *ex-situ* annealed at 170 ^{o}C for 3 hours, and then imaged; (a) without and (b) with crossed-polarizers. The scale bar is 20μm.

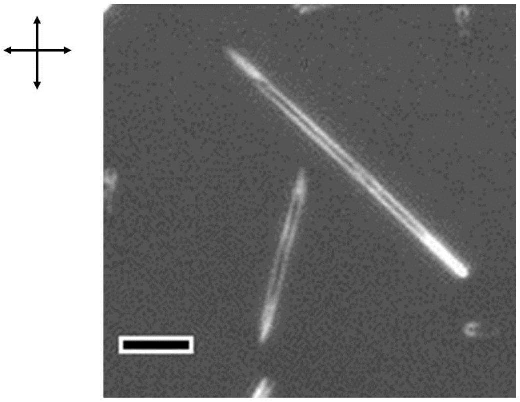

Figure S9. Zoomed in image from fig. S8b showing the correspondence between intensity and height *within* the needles. The scale bar is 5μm.

Optical microscopy under crossed-polarizers reveals birefringence, with a clear correlation between the light intensity under crossed-polarizers, and both the needle orientation (fig. S8) and the height profile *within* the needles (fig. S9 in comparison with fig. S4 and fig. 1d), as expected for a single crystal.

1.4 Growth-Rate Dependence on Annealing-Time.

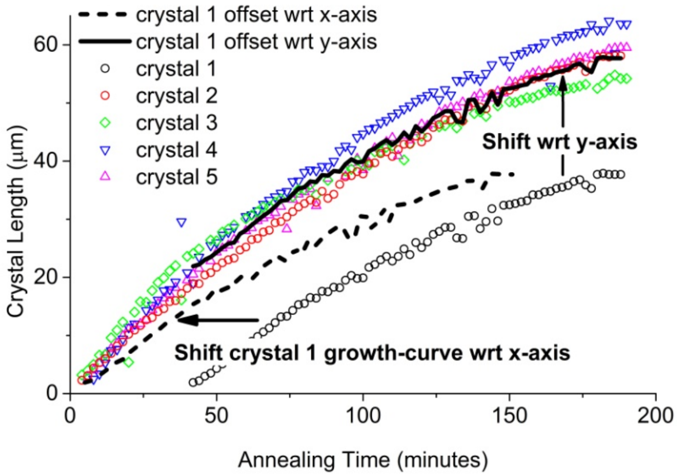

Figure S10. *In-situ* optical microscopy growth-curves at 170 °C for a selection of crystals in a 20nm PCBM/35nm 344k PS sample.

Fig. S10 plots growth-curves from a single sample, showing 4 crystals that nucleate after around 5 minutes annealing, plus a crystal that nucleates after about 40 minutes (this is the same data that is shown in fig. 2d). We also show the growth-curve for this later-nucleated crystal shifted in two different ways; i) by the addition of a constant length to this data-set (shifting with-respect-to the y-axis) and ii) by the subtraction of a constant time (shifting with-respect-to the x-axis) from this data-set. The close match between the shape of the growth-curve shifted wrt the y-axis and the growth-curves for the other crystals, and the poor match when the curve is shifted wrt the x-axis, suggests that the gradual decline in growth-rate of the crystals is a function of the annealing-time, rather than of the time since nucleation began. This dependence of growth-rate on annealing time, rather than time-since-nucleation is apparent in later-nucleated crystals in a number of 344k and 106k bilayers, of PS thickness of 35nm or larger (data not shown).

1.5 Composition Profiles from NR.

In-situ annealed samples

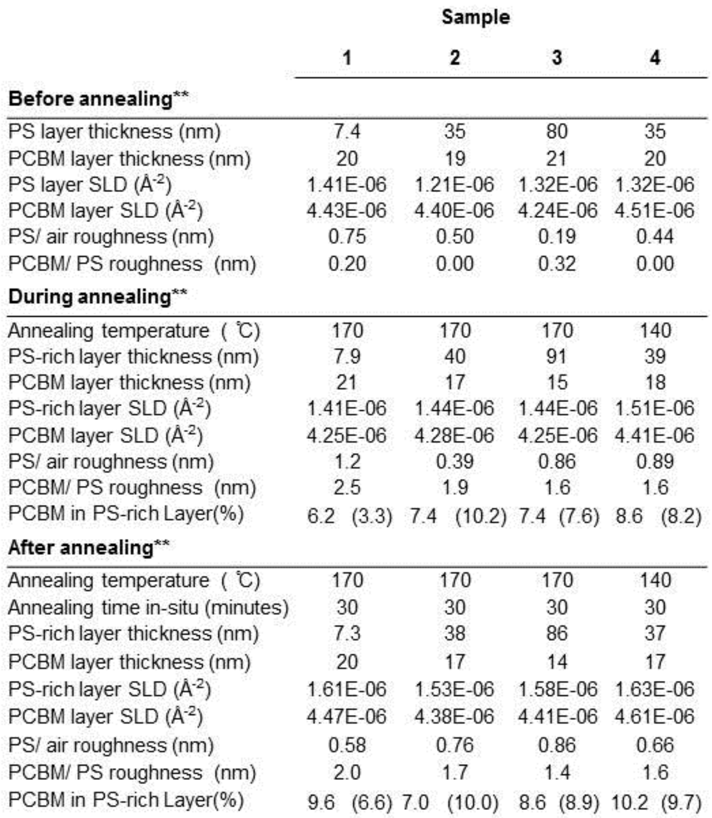

	Sample			
	1	**2**	**3**	**4**
Before annealing**				
PS layer thickness (nm)	7.4	35	80	35
PCBM layer thickness (nm)	20	19	21	20
PS layer SLD (Å^{-2})	1.41E-06	1.21E-06	1.32E-06	1.32E-06
PCBM layer SLD (Å^{-2})	4.43E-06	4.40E-06	4.24E-06	4.51E-06
PS/ air roughness (nm)	0.75	0.50	0.19	0.44
PCBM/ PS roughness (nm)	0.20	0.00	0.32	0.00
During annealing**				
Annealing temperature (°C)	170	170	170	140
PS-rich layer thickness (nm)	7.9	40	91	39
PCBM layer thickness (nm)	21	17	15	18
PS-rich layer SLD (Å^{-2})	1.41E-06	1.44E-06	1.44E-06	1.51E-06
PCBM layer SLD (Å^{-2})	4.25E-06	4.28E-06	4.25E-06	4.41E-06
PS/ air roughness (nm)	1.2	0.39	0.86	0.89
PCBM/ PS roughness (nm)	2.5	1.9	1.6	1.6
PCBM in PS-rich Layer(%)	6.2 (3.3)	7.4 (10.2)	7.4 (7.6)	8.6 (8.2)
After annealing**				
Annealing temperature (°C)	170	170	170	140
Annealing time in-situ (minutes)	30	30	30	30
PS-rich layer thickness (nm)	7.3	38	86	37
PCBM layer thickness (nm)	20	17	14	17
PS-rich layer SLD (Å^{-2})	1.61E-06	1.53E-06	1.58E-06	1.63E-06
PCBM layer SLD (Å^{-2})	4.47E-06	4.38E-06	4.41E-06	4.61E-06
PS/ air roughness (nm)	0.58	0.76	0.86	0.66
PCBM/ PS roughness (nm)	2.0	1.7	1.4	1.6
PCBM in PS-rich Layer(%)	9.6 (6.6)	7.0 (10.0)	8.6 (8.9)	10.2 (9.7)

Ex-situ annealed samples

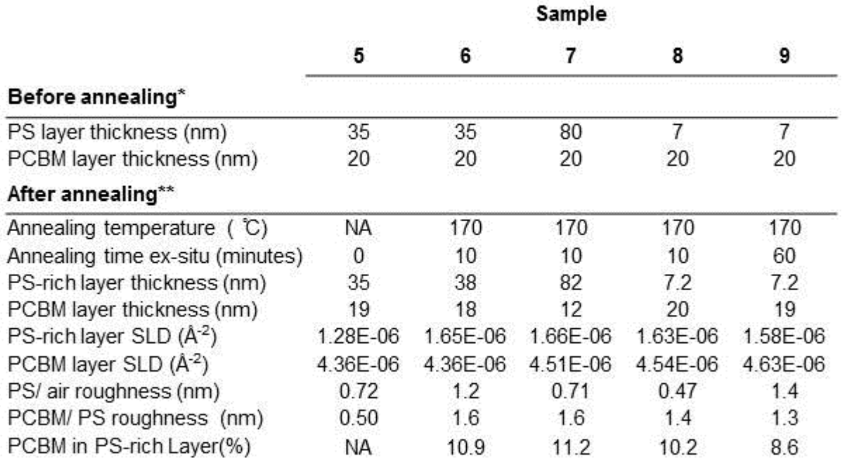

	Sample				
	5	**6**	**7**	**8**	**9**
Before annealing*					
PS layer thickness (nm)	35	35	80	7	7
PCBM layer thickness (nm)	20	20	20	20	20
After annealing**					
Annealing temperature (°C)	NA	170	170	170	170
Annealing time ex-situ (minutes)	0	10	10	10	60
PS-rich layer thickness (nm)	35	38	82	7.2	7.2
PCBM layer thickness (nm)	19	18	12	20	19
PS-rich layer SLD (Å^{-2})	1.28E-06	1.65E-06	1.66E-06	1.63E-06	1.58E-06
PCBM layer SLD (Å^{-2})	4.36E-06	4.36E-06	4.51E-06	4.54E-06	4.63E-06
PS/ air roughness (nm)	0.72	1.2	0.71	0.47	1.4
PCBM/ PS roughness (nm)	0.50	1.6	1.6	1.4	1.3
PCBM in PS-rich Layer(%)	NA	10.9	11.2	10.2	8.6

Table S1. NR fit parameters for unannealed (sample 5), *in-situ* annealed and *ex-situ* annealed bilayers. * Layer thickness obtained before annealing by AFM, ** Fit parameters obtained from NR. The % PCBM in the PS-rich layer for the *in-situ* annealed samples was calculated using two different methods (details given in the 'Methods; Further Details' section at the end of this document). The results of method 1 are given first, with the results of method 2 in brackets.

Table S1 gives NR fit parameters for *in-situ* and *ex-situ* annealed PCBM/PS bilayers. The PCBM content within the PS-rich layers (calculated from samples 1-4 and 6-9 after annealing using method 1 – see the 'Methods; Further Details' section at the end of this document) is 9.5 ± 1.4 %, and the PCBM/PS-rich-layer interface roughness is 1.6 ± 0.2nm. Figs S11a and S11b show the NR and fitted SLD profiles for two duplicate PCBM/PS (7nm) bilayer samples *ex-situ* annealed for 10 and 60 minutes showing, in agreement with the findings from *in-situ* annealing (figs 3a and 3d), that the equilibration process is complete after 10 minutes or earlier, resulting in an interface of roughness ~1.4nm between PCBM and a PS-rich phase containing ~ 9-10% PCBM. Figures S11c and S11d show the evolution of the reflectivity and SLD profile during the first 4 minutes of heating at ~170 ^{o}C. The *in-situ* reflectivity curves in fig. S11c, in common with the observations for other samples (see fig. 3), show a reduction in reflectivity and the emergence of stronger features with a smaller fringe spacing. This is a clear signature of reduced contrast at the buried-interface within the bilayer, giving a smaller amplitude for reflection, and therefore greater visibility of the fringe spacing due to the total bilayer thickness. Changes in the SLD profile are complete within 3-4 minutes (i.e. before the sample surface temperature reaches its maximum value of 170 ^{o}C - see fig. S20). However, even though the *in-situ* measurements are not able to capture the isothermal kinetics of interface broadening, they do allow us to conclude that the rapid changes in the composition-profile occur while the temperature is still rising, and that the composition-profile remains unchanged as the temperature then reaches a peak of ~170 ^{o}C before settling to a steady value of 164 ^{o}C.

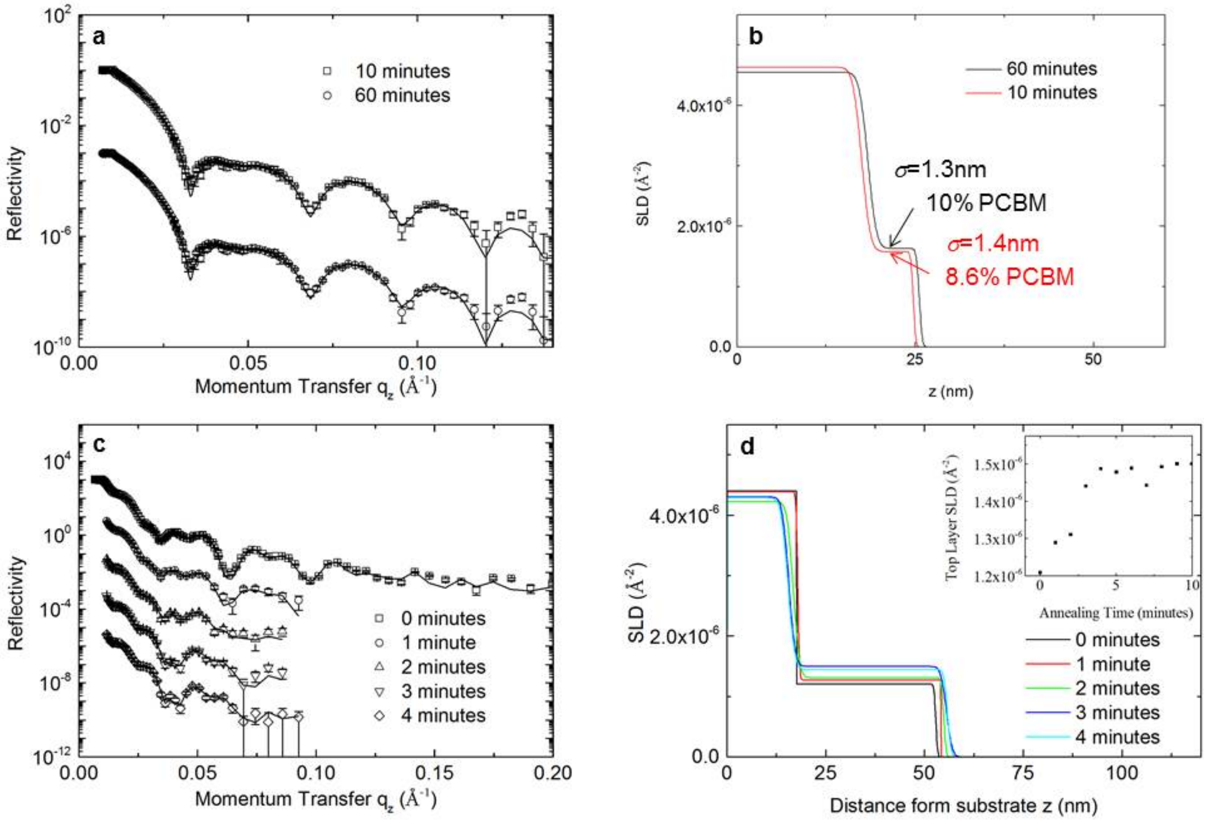

Figure S11. (a) NR and (b) SLD profiles from PCBM/PS(7nm) samples annealed for 10 and 60 minutes at 170 ^{o}C and measured *ex-situ*. (c) NR and (d) SLD profiles from a PCBM/PS(35nm) bilayer annealed at 170 ^{o}C and measured *in-situ*. Reflectivity curves are offset for clarity.

In-situ annealing allows the reflectivity to be modeled from a known starting composition-profile, from which the subsequent profile-evolution can be followed in small steps. By measuring the change in SLD in an *in-situ* annealed PCBM single-layer due to thermal expansion, and using literature measurements of thermal expansion in thin PS films,[3] we were able to account for the small density changes during annealing. This allowed us to estimate the PCBM concentration within the PS-rich layer *during* annealing (albeit with less accuracy than the before/after annealing measurements, because of the restricted q_z range). The composition profiles obtained from the *in-situ* samples measured at 80 ^{o}C after cooling were very similar to those obtained during annealing, and to those obtained for the *ex-situ* annealed samples (see table S1). Mixing in P3HT/PCBM bilayers occurs on a similarly rapid time frame (of a few minutes) to that in the PCBM/PS system and then remains unchanged. The reflectivity curve and SLD-profile for a PCBM/P3HT sample after 1 hour at 140 ^{o}C is shown in fig. S12.

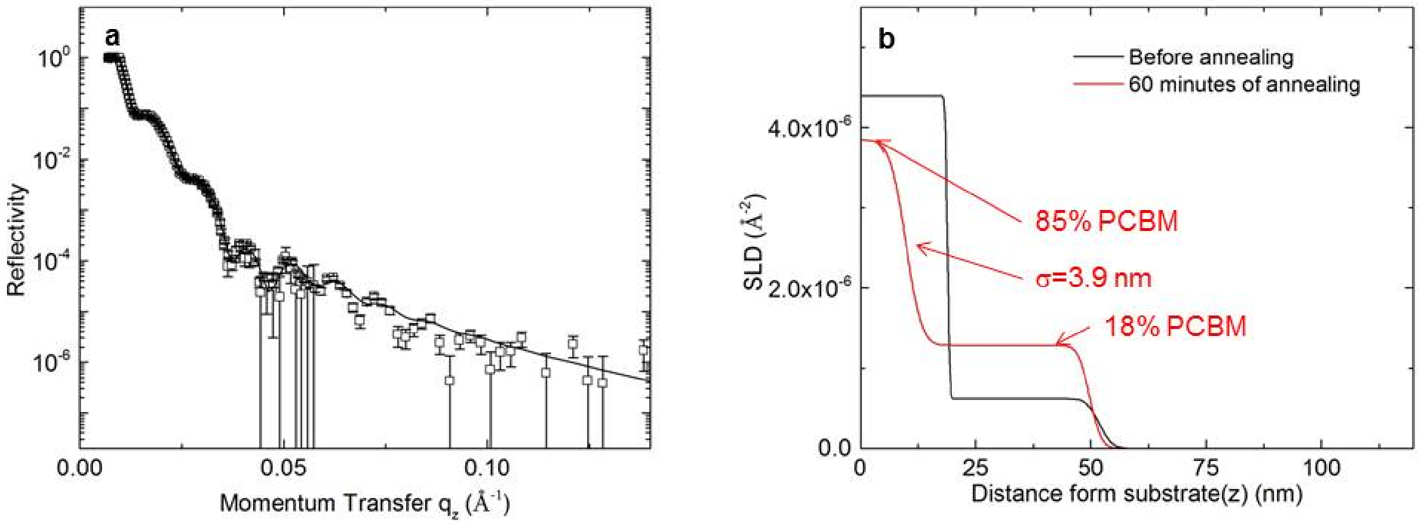

Figure S12. (a) NR from a PCBM(20nm)/P3HT(40nm) bilayer annealed at 140 °C for 60 minutes and measured *ex-situ*. (b) SLD profiles for this sample before and after annealing.

1.6 Growth-Curve Independence from PCBM Layer Thickness Changes.

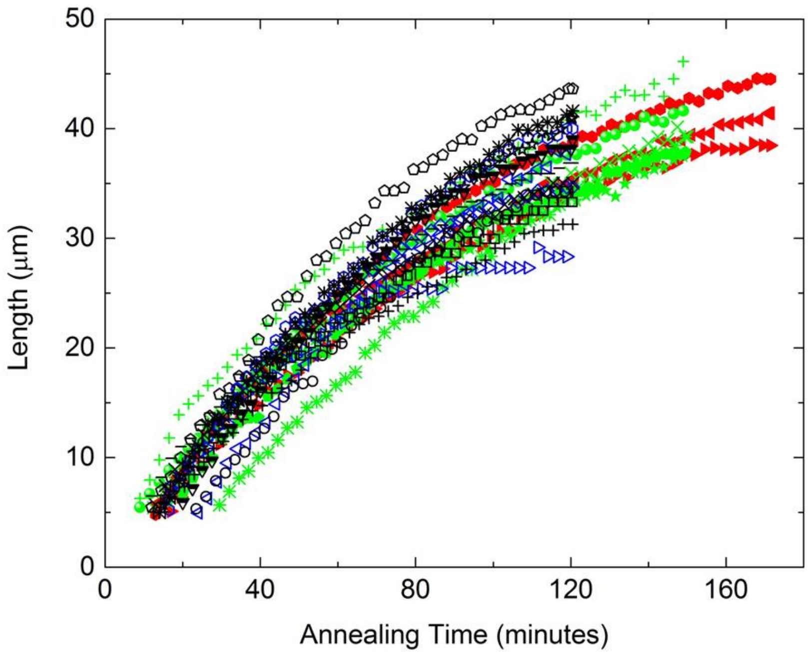

Figure S13. *In-situ* optical microscopy growth-curves at 170 °C for a selection of crystals in different PCBM thickness samples, all with a 35nm 344k PS layer on top; 14nm PCBM (red), 17nm PCBM (green) and two different samples with 20nm PCBM (black and blue). This data was obtained using a mercury-lamp illumination source.

As PCBM migrates into the PS layer, the thickness of the remaining PCBM layer reduces in proportion to the thickness of the PS layer (see fig. 3 and table S1). This is most significant for the thicker PS layers and so would not be expected to be a factor in the observed thickness-dependent behavior shown in fig. 6. To confirm this we fabricated bilayers with PCBM layers than were thinner than the 20nm used throughout the rest of this study. Fig. S13 shows that this reduction in PCBM thickness has no effect on the needle-like crystal growth behavior. Fig. S13 also illustrates the degree of variation in crystal growth-curves from sample-to-sample and crystal-to-crystal (within a single sample).

1.7 GIXD Above and Below the Critical Angle and Crystalline Volume-Fraction Estimation.

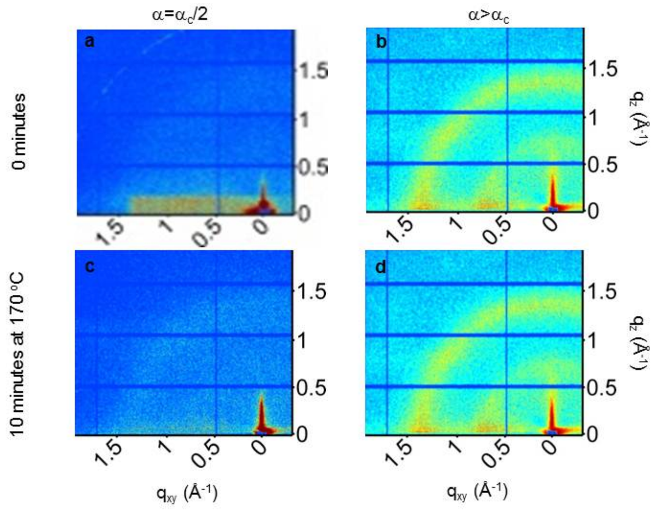

Figure S14. GIXD intensity maps for unannealed ((a) and (b)) and annealed ((c) and (d)) PCBM(20nm)/344k-PS(120nm) bilayers above and below the critical angle α_c (~0.1°).

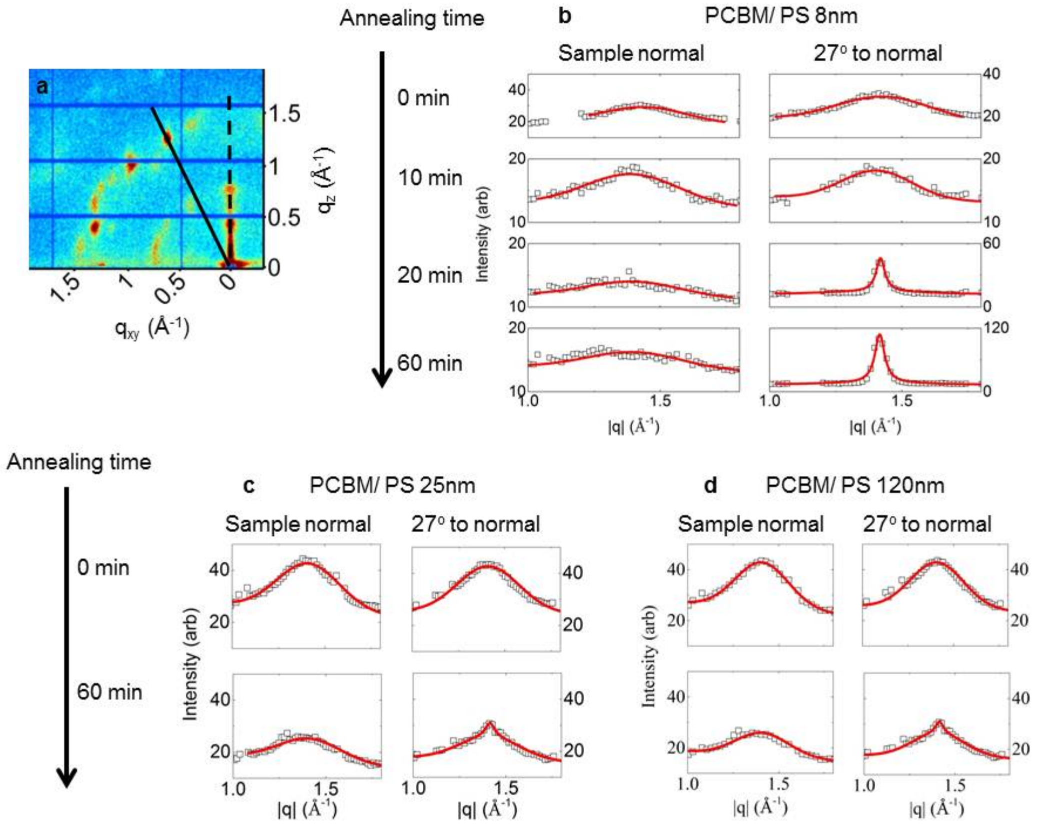

Figure S15. Line-profiles through GIXD detector maps. (a) A detector map for 8nm PS after 60 minutes annealing, showing the directions of the two profiles; i) along the sample normal (dashed line), ii) at 27° to the sample normal (solid line). (b)-(d); intensity-profiles normal to the sample (right-hand figure for each PS-thickness and annealing-time) and at an angle of 27° to the sample (left-hand figure for each PS-thickness and annealing-time) for bilayer samples with 3 different PS thicknesses, at several annealing times at 170°C. The red lines are fits using equation S2. The PCBM thickness was 20nm and 344k-PS was used in all samples

GIXD maps above and below the critical angle were very similar for both 8nm and 25nm PS bilayers. However, for the unannealed 120nm PS bilayers there was very little intensity at the location of the PCBM amorphous rings below the critical angle (see fig. S14a), due to the PS film being significantly thicker than the penetration depth of the evanescent wave (of order ~10nm). After 10 minutes annealing the intensity of the amorphous PCBM rings is now just about visible in this bilayer (fig. S14c). This further corroborates the finding from NR of movement of a small amount of PCBM into the PS layer on annealing.

Figure S15 shows line-profiles through GIXD intensity-maps for different PS-thickness bilayers at various annealing-times. The line-profiles show the intensity integrated over a 5^{o} sector as a function of the (approximate) magnitude of momentum transfer, $|\underline{q}|$, along two directions (as described in Lilliu *et al.*[5]); i) through a prominent crystalline PCBM peak and ii) through a region of $|\underline{q}|$ space that only contains scattering from amorphous PCBM. The integrated intensity profiles were fitted using the methodology described in the Methods; Further Details section at the end of this supplementary information document. The extracted fit parameters for the width and intensity of the crystalline and amorphous peaks were used to provide an upper and lower estimate of the crystalline and amorphous fractions of the PCBM nanocrystals within the samples, and the size of the PCBM crystallites (see Methods; Further Details below). Figure S16 plots the estimates for crystalline volume-fraction as a function of annealing-time and also shows fits to this data using equation S4, for three different thicknesses of PS.

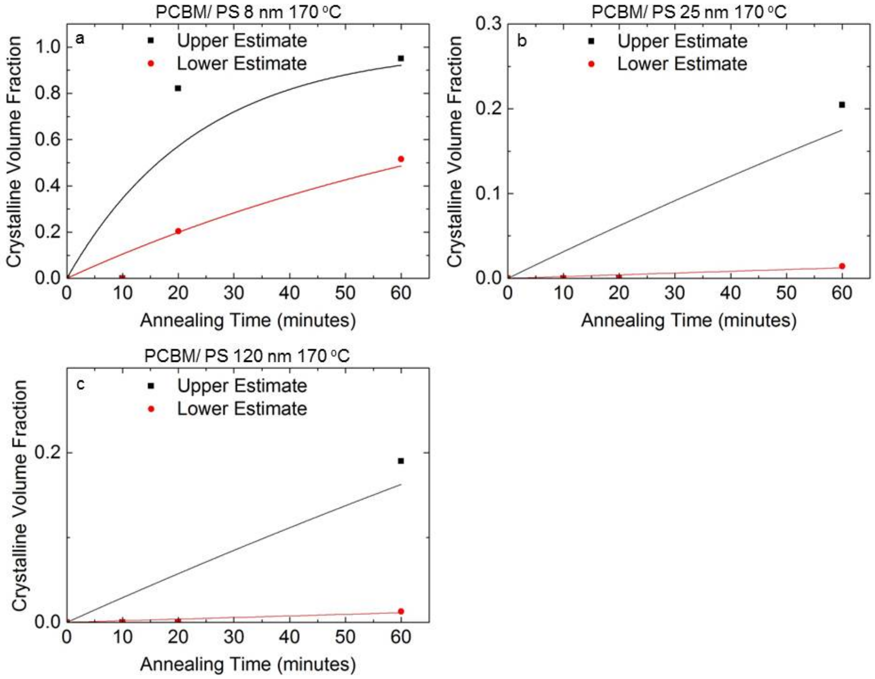

Figure S16. Upper and lower estimates of the crystalline PCBM volume-fraction calculated from GIXD, as a function of annealing-time at 170 ^{o}C for 344k-PS-film-thicknesses of (a) 8nm, (b) 25nm and (c) 120nm. The lines are Avrami fits (equation S4) to these three data sets (with n=1). The PCBM thickness was 20nm in all samples.

1.8 Bilayers Annealed on Mica Substrates.

Figs S17a–c show optical microscopy images of micron-sized PCBM crystals found in three different areas of a PCBM/PS bilayer sample that was annealed on a mica substrate and then imaged. These images show the existence of needle-like crystals and isotropic crystals. There is significant variability in the morphology, in terms of the relative density of the needle-like and isotropic crystals. The cause of this variability isn't clear at present. However, the influence of the mica substrate is apparent. The cubic PCBM crystals that we observe in PCBM/P3HT bilayers on mica exhibit similar behavior to that observed by Zheng et al[6], in which the crystals adopt specific orientations in the plane of the mica substrate (fig. S17d shows cubic crystals adopting three specific orientations that are templated by the mica substrate).

TEM was performed on samples that were annealed on mica for 2 and 24 hours. For the samples that were annealed for 2 hours at 170 ^{o}C, SAED was used to examine the samples in regions between the visible crystals. No diffraction peaks or rings were observed.

The *d*-spacings (the spacing between Bragg planes given by the electron wavelength divided by 2Sinθ, where θ is the Bragg angle) for the SAED inset in fig. 5c, are 1.50, 1.01, 0.88, 0.83, 0.59, 0.49 and 0.42nm. The *d*-spacings in fig. 5f are 1.47, 0.91, 0.83, 0.5 and

0.44nm. *d*-spacings similar to these are found in the literature by TEM and x-ray diffraction, for PCBM crystals formed on mica[7] and silicon/silicon-oxide substrates.[8]

Energy dispersive x-ray spectroscopy was performed in the TEM on the different crystal forms observed, as well as in the regions between the crystals. This showed the presence of carbon and oxygen only, confirming the absence of any inorganic contaminant material in the specimen.

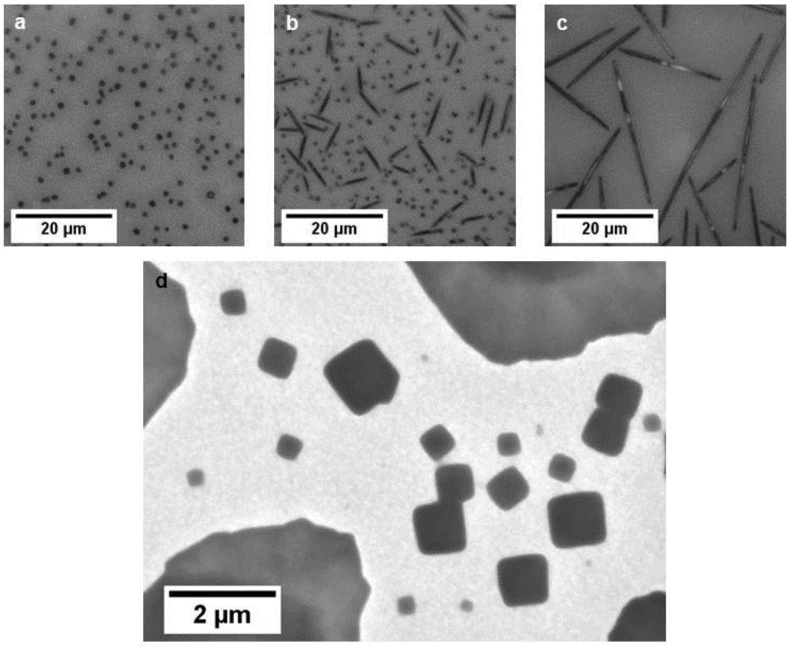

Figure S17. (a)-(c) Optical microscopy images of PCBM crystals after annealing a PCBM(20nm)/344k-PS(35nm) bilayer on a mica substrate for 120 minutes at 170 ^{o}C ((a), (b) and (c) are on different areas of the same sample). d TEM image of a PCBM(20nm)/P3HT(40nm) bilayer annealed at 140 ^{o}C for 24 hours, showing an area of the sample containing cubic crystals.

2. Methods; Further Details.

2.1 Error Estimation.

Except for figs 6b, 6c, S1, S2, S6 and S19, all errors quoted or shown in figures in the manuscript and supplementary information are (±) the standard deviation. In figs 6b, 6c, S1, S2, S6 and S19 the data points are the means of nominally identical repeated measurements and the error bars represent (±) the standard error of the mean.

2.2 AFM; Layer Thickness.

PCBM and polymer layer thickness was determined by scratching the surface of single-layers on silicon substrates and measuring across the edge of the scratch using AFM, (this was corroborated by NR measurements on some of the samples).

2.3 Optical Microscopy.

ImageJ (NIH USA) was used to extract intensity profiles along the dominant growth direction of individual crystals for *in-situ* annealed samples. Only straight crystals that were not visibly impeded by other crystals or imperfections on the sample surface were used. The intensity profiles were first re-zeroed by displacement along the ordinate so that the mean intensity in the flat part of the profile (the part undisturbed by the crystal) was zero. The length was then measured between the two growing fronts of the crystal, defined as the positions where the magnitude of the intensity was at half the average intensity within the crystal ('within the crystal' was defined as all locations along the profile where the magnitude of the intensity, after re-zeroing was above a fixed threshold; see fig. S18). The use of alternative methods in which crystal-lengths were calculated i) using an absolute intensity threshold, and ii) 'manually', by measuring individual crystals by eye, gave almost identical growth-curves. This 'manual' approach was utilized to extract half-crystal growth curves (measuring the length from the nucleation point to one end of the crystal) for very long crystals, in which only one end of the needle remained isolated from other crystals at long annealing times (as occurred for 35nm and 60nm 106k PS samples).

The number of crystals per unit area and the mean area per crystal for samples that were annealed and then imaged *ex-situ*, (figs S1 and S2) were calculated using the built-in 'Auto Threshold' and 'Particle Analyzer' commands in ImageJ. Isotropic crystals were not included in this analysis. The means and error bars were calculated using images from several different areas of each sample.

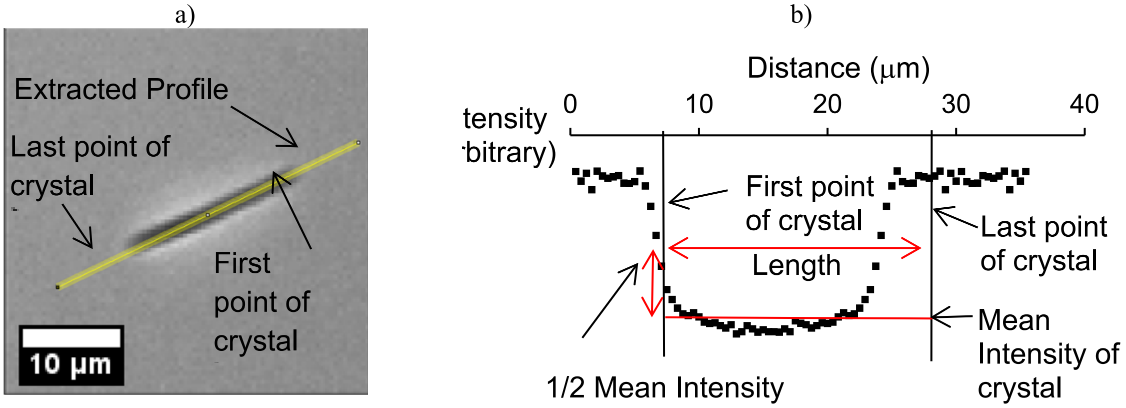

Figure S18. Crystal length calculation. (a) Optical micrograph of crystal. (b) Intensity profile along crystal showing length calculation methodology for a crystal of length 18.1μm.

Mercury lamp illumination; Given the potential sensitivity of fullerenes to UV and visible light, we probed the influence of the microscope lamp illumination spectrum by repeating our *in-situ* optical microscopy experiments using a mercury lamp (with a 500nm dichroic mirror) on the microscope (again, keeping the incident intensity as low as possible). In contrast to the tungsten-halogen lamp, this illuminated the sample with UV light, as well as some visible light. The results from measurements on 75 different crystal growth-curves are shown in fig. S19. The results show the same overall behavior as that shown in figs 2 and 6. The only notable difference is the lower growth-rates of the 106k-PS crystals for thicknesses of 35nm and larger (fig. S19b), in comparison to the growth-rates in fig. 2c. Further investigation is required to understand the origin of this difference. Simultaneous fitting of the 75 datasets, using the integral of equation (1) with the fit parameter n fixed at 1, and the parameters m and ϕ_m the same for all datasets, resulted in A parameters (fig. S19e) that showed similar behavior to fig. 6b (i. e. showing little clear thickness-dependence, but an indication of higher values for the 106k-PS bilayers). We note that the numerical values of the A parameter in fig. S19e are lower than those in fig. 6b. This is due in-part to the different values of the fit parameter m in the two simultaneous fits. We can still obtain good fits if the mercury-lamp data and the tungsten-halogen-lamp data are both fitted with m and ϕ_m restricted to have the same value. In this case the numerical values of the fitted A parameters in the mercury-lamp data and the tungsten-halogen-lamp data are much closer. However, it is clear from fig. S19f that, despite any differences in the other fit parameters, the K parameters show very similar thickness-dependent and M_w-dependent behavior and also similar numerical values to the tungsten-halogen-illuminated data in fig. 6c. This gives us further confidence in the robustness and independence from microscope illumination of our findings regarding the nanocrystal growth-rate parameter K.

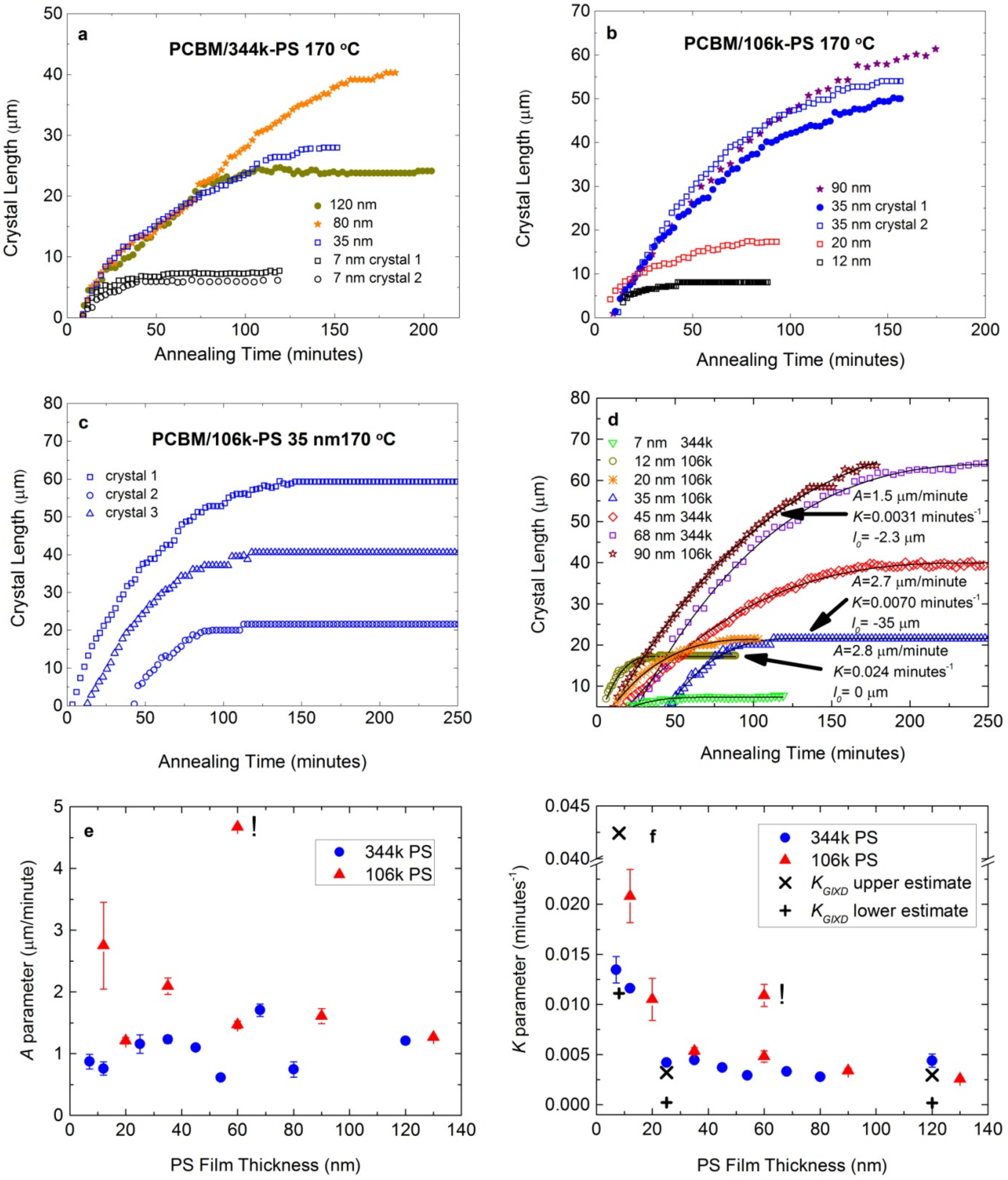

Figure S19. *In-situ* isothermal growth of isolated PCBM crystals, and simultaneous fit results for silicon/PCBM/PS bilayers annealed at 170 °C (mercury-lamp illumination). All samples have a 20nm PCBM bottom layer with (a); a 344k-PS top layer and (b)-(c); a 106k-PS top layer. Figs (a) and (b) show a selection of crystals that nucleate at approximately the same time, for various PS thicknesses. Fig. (c) shows crystals that nucleate after different annealing-times on a single sample. The labels crystal 1 - crystal 3 represent different crystals on the same sample. (d) Optical microscopy growth-curves and fits for a selection of the 75 simultaneously-fitted PCBM needles that have nucleated at various times and then grown in different M_w and thickness PS bilayers. These fits had the following equation (1) fit parameters shared by all 75 datasets; n=1 (fixed), m=1.34, ϕ_m=0.58. (e)-(f) fit parameters A and K respectively, as a function of PS thickness and M_w. Fig. S19f also shows upper and lower estimates of the Avrami growth-rate parameter extracted from the GIXD data in fig. 4, K_{GIXD}, as a function of PS thickness for 344k-PS. We have a suspicion that the sample marked with an exclamation mark in figs (e)-(f) may have been annealed by mistake at 180 °C, rather than at 170 °C, but we include the data for completeness.

2.4 GIXD Data Analysis.

The components of the momentum transfer vector ($\underline{q}$) are

$$q_x = k(cos\alpha_i - cos\alpha_f cos\gamma), \quad \text{(S1a)}$$

$$q_y = ksin\gamma, \quad \text{(S1b)}$$

$$q_z = k(sin\alpha_i + sin\alpha_f), \quad \text{(S1c)}$$

where k is the magnitude of the wavevector, α_i and α_f are the out-of-plane incident and exit angles respectively, and γ is the in-plane exit angle.[9] The GIXD intensity maps shown in figs 4 and S14 are direct detector maps. In common with previous workers[2,10] the intensity map axes are labeled q_z and q_{xy}, with q_z as given in equation S1c above, and q_{xy} defined as $(q_x^2 + q_y^2)^{1/2}$ with q_x evaluated using equation S1a with $\alpha_f = -\alpha_i$ (i.e. for q_z=0). Profiles were extracted from the detector maps and fitted using Origin Pro 9 to obtain peak widths, centers and areas.

Estimation of amorphous and crystalline PCBM fractions; Profiles were extracted from the detector map along i) a line normal to the sample (at constant q_{xy}) and ii) along a line at β = 27 to the sample normal using the computer code GI-XRD-GUI used by Lilliu et al.[5] The profile along the normal to the sample contained no crystalline peak, while the β = 27 profile passed through one of the highest-intensity PCBM crystalline peaks to emerge from within the amorphous ring at $|\underline{q}| \sim 1.5$ Å^{-1} on annealing (see fig. S15a). Both profiles were integrated over a 5 wide sector centered on the direct beam.

Following the methodology of Jukes et al,[11] the intensity of each profile between 1 and 1.8 Å^{-1} was fitted using the sum of a Gaussian and a Lorentzian peak, representing the amorphous and crystalline contribution to the scattering respectively. The fitting function, representing the sum of these peaks is:

$$I(q) = B_0 + B_1 q + A_G\left(\frac{2\eta}{\pi W_G^2}\right)^{1/2} exp\left(-\frac{1}{2}\frac{\eta(q-Q_G)^2}{(W_G/2)^2}\right) + A_L\frac{1}{\pi}\frac{W_L/2}{(W_L/2)^2 + (q-Q_L)^2}, \quad \text{(S2)}$$

where q is the magnitude of the approximate momentum transfer ($q=|\underline{q}|=(q_{xy}^2 + q_z^2)^{1/2}$) and η=2ln2. The parameters B_0 and B_1 represent a linear sloping background. The parameters A_G, W_G, Q_G and A_L, W_L, Q_L are the area, full-width half maximum (FWHM) and maximum location (q) of the Gaussian and Lorentzian peaks respectively. The parameters W_G and Q_G were determined by fitting the unannealed sample. Then for each annealed sample the (amorphous) profile normal to the sample was fitted first, using only the background terms in S2 and A_G as fitting parameters. The Gaussian parameters obtained from this fit were then fixed during the fitting of the β = 27 profile. For all samples the parameter Q_L was fixed at the value obtained for the 8nm PS sample after 60 minutes annealing, allowing the Lorentzian (A_L and W_L) and background terms to be determined for all annealed samples. The crystalline volume fraction, ϕ_{GIXD}, was then determined using:

$$\varphi_{GIXD} = \frac{A_L}{(A_G + A_L)}. \quad \text{(S3)}$$

The value of ϕ_{GIXD} for each sample was plotted against annealing-time, t, (fig. S16) and fitted with the following (n=1) Avrami equation[12]

$$\varphi_{GIXD}(t) = 1 - exp(-K_{GIXD}t) \quad \text{(S4)}$$

to obtain an estimate of the K_{GIXD} parameter. This procedure gives an upper estimate for the value of ϕ_{GIXD} at each annealing-time, and therefore an upper estimate for K_{GIXD}. This is because estimating ϕ_{GIXD} using the line profile analysis described above assumes that the diffraction pattern is isotropic (powder diffraction). Given our anisotropic diffraction pattern, indicating a preferential alignment of the nanocrystals with respect to the substrate, the integration over a 5° sector centered on a crystalline peak will underestimate the amount of amorphous scattering. To give a lower-bound estimate for ϕ_{GIXD} we multiplied the fitted Gaussian area from the line profile analysis by a factor of 18 (90°/5°) and re-calculated ϕ_{GIXD} The lower estimate ϕ_{GIXD} values were then fitted using equation S4 to obtain a lower estimate for K_{GIXD}.

Scherrer analysis; The fitted profiles at 27° were also used to extract the crystallite size (d) using the Scherrer equation[13,14]

$$d = \frac{K\lambda}{B\cos(\theta_B)}, \quad \text{(S5)}$$

where λ is the x-ray wavelength (1.3Å), K is a constant (assumed to by 0.9), θ_B is the Bragg angle of the Lorentzian peak and B is the FWHM of the Lorentzian peak, converted into radians. While the absolute values of the crystallite sizes depend upon the value of K used in the Scherrer relation, the values of d give an order-of-magnitude estimate of the size of the PCBM crystallites, and also allow comparison of the crystallite sizes for different PS thicknesses. Mean values for d and an estimate of the error were calculated by repeating this analysis using line-profiles extracted from the detector map through crystalline peaks at several other angles.

2.5 NR; Further Experimental Details.

A full reflectivity curve (at incident angles of 0.6° and 2.4°) was obtained for *ex-situ* annealed samples. Reflectivity data was collected from *in-situ* annealed bilayers before, during and after annealing, as follows;

1) Samples were clamped to a hot plate within a purpose-built annealing chamber located in the neutron beam path, and the chamber was flooded with a continuous flow of nitrogen. The hot plate temperature was set to 80°C. After allowing the sample temperature to stabilize a full reflectivity curve was obtained.[15]

2) After completion of this measurement the hot plate set point was changed to 142 °C or 174 °C, and reflectivity curves were collected repeatedly at an incident angle of 1°, with the data binned into 30 seconds slices.

3) After 30 minutes of annealing the set point of the hot plate was changed to 80°C and, after allowing sufficient time for the sample to cool down to this temperature (this took around 15 or 20 minutes for cooling from 140 °C or 170 °C respectively), another full reflectivity curve was obtained.

The set point of the hot plate differed from the sample surface temperature significantly at high temperatures. The relationship between set point, sample temperature and time was calibrated by attaching a thermocouple to the surface of a duplicate Si block at the two set points used (see fig. S20).

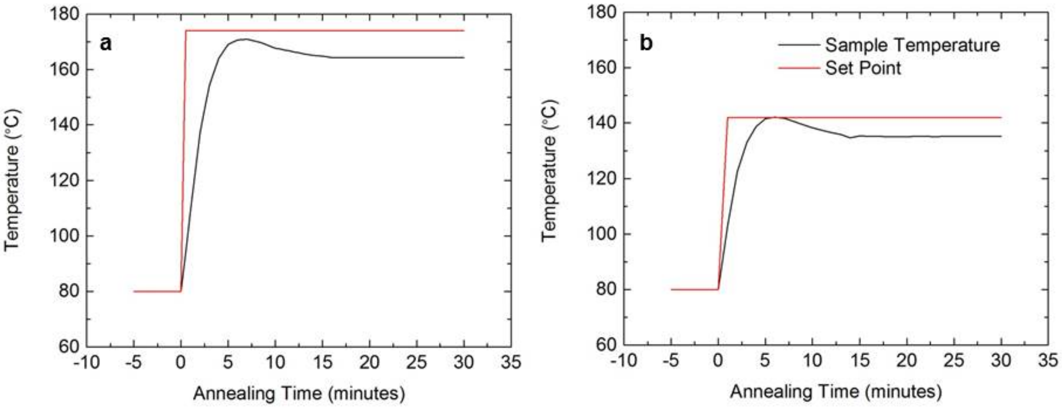

Figure S20. Heating block thermocouple temperature (Set Point) and sample temperature versus time for *in-situ* NR at set points of (a) 174 °C and (b) 142 °C.

Specular reflectivity was fitted using Parrat32 (Hahn-Meitner-Institut, Berlin Neutron Scattering Centre, Berlin, Germany) to fit the parameters of a multi-layer model to the reflectivity of each sample using a least-squares-fit approach. The model parameters were the thickness and scattering length density (SLD) of each layer and the (Gaussian) interfacial roughness, σ, between adjacent layers. This roughness parameterizes the width of an interface assuming an error-function profile.[16,17] NR measures the SLD-profile of the sample averaged over a lateral distance (i.e. in the plane of the sample) of order tens-of-microns (the in-plane coherence length of the neutrons)[17]. The instrumental resolution was included within the models for all samples, at the values calculated from the slit widths and chopper settings.[18]

The silicon substrate SLD was fixed at 2.07 x 10^{-6} Å^{-2}, given the known density of silicon. The silicon substrate roughness was fixed at 0.7nm. The native silicon oxide layer parameters were first fitted for several different samples, resulting in average values as follows; SLD = 3.48 x 10^{-6} Å^{-2}, thickness = 1.5nm and roughness = 0.7nm. All samples were then fitted with the native silicon oxide layer parameters fixed at these values. The thickness and surface roughness of PCBM, PS and P3HT layers in unannealed samples were also obtained by measuring single layers using an AFM. Good agreement was found between NR and AFM measurements.

The SLD for PCBM was obtained from fits of single layers. The SLDs for P3HT and PS were calculated using the National Institute of Standards and Technology SLD calculator (http://www.ncnr.nist.gov/resources/sldcalc.html) with literature density values.[19,20] These values were used as initial guesses when fitting the reflectivity curves of unannealed bilayers, and *ex-situ* annealed bilayers. For *in-situ* samples the fit parameters from the previous time slot in the kinetic series were used as the initial guesses. Our measured SLD values obtained from the single layer and unannealed bilayer fits were found to be in good agreement with reported literature values.[20,21] The percentage (by volume) of PCBM in the PS-rich layer was calculated as;

100 x ($\mathrm{SLD}^{\text{PS-rich layer}}$-$\mathrm{SLD}^{\text{Pure PS}}$)/($\mathrm{SLD}^{\text{Pure PCBM}}$- $\mathrm{SLD}^{\text{Pure PS}}$), where $\mathrm{SLD}^{\mathrm{i}}$ is the SLD of layer i.

This percentage was calculated for each annealed bilayer sample using two methods. Method 1 took $\mathrm{SLD}^{\text{Pure PS}}$ and $\mathrm{SLD}^{\text{Pure PCBM}}$ as the average SLD of the PS and PCBM layers respectively, in samples 1 to 4 before annealing. Method 2 took $\mathrm{SLD}^{\text{Pure PS}}$ and $\mathrm{SLD}^{\text{Pure PCBM}}$ as the SLD of the PS and PCBM layers respectively, from the specific sample in question before annealing. A similar methodology was used for the PCBM/P3HT samples, with the pure PCBM SLD taken from the specific sample in question before annealing, and the pure P3HT SLD calculated from the NIST SLD calculator.

2.6 Crystal Growth-Curve Model and Data Analysis; Further Details.

The Avrami model has been used successfully to model the isothermal growth of the crystal volume-fraction in a wide range of materials including polymer/fullerene nanocomposites.[2,22,23] The model gives the crystalline volume fraction, ϕ, as a function of time, t, as follows;

$$\varphi(t) = 1 - e^{-(Kt)^n}, \qquad \text{(S6)}$$

where K and n are the Avrami rate-constant and exponent respectively. We modeled the increasing nanocrystal content of the PCBM film using equation S6. As $\phi(t)$ increases the viscosity of the PCBM layer will increase, as a result of the higher solids fraction. Findings from suspension rheology suggest that the viscosity will rise significantly above that in the absence of suspended solid particles for ϕ greater than approximately 0.1-0.2 for a range of different solid particle shapes.[24] Eventually the solid particles will percolate across the material and 'jam' at a volume-fraction of solids ϕ_m. The value of ϕ_m at which this jamming occurs, and the viscosity diverges, ranges from ~0.23 for high aspect ratio rods up to ~0.71 for spheres. A theoretical treatment of the way in which the suspension viscosity increases with ϕ was given by Krieger and Dougherty.[24,25] The Kreiger-Dougherty equation for the suspension viscosity, η, is given as

$$\eta(\varphi) = \eta_s\left(1 - {}^{\varphi}\!/_{\varphi_m}\right)^{-[\eta]\varphi_m}, \qquad \text{(S7)}$$

where η_s is the viscosity of the fluid in the absence of suspended solid particles, and $[\eta]$ is the intrinsic viscosity of the suspension (a dimensionless quantity that is a function of the shape of the suspended particles).[24] Substitution of $\phi(t)$ from equation S6 into equation S7 gives $\eta^{-1}(t)$ of the form

$$\eta(t)^{-1} = \eta_s^{-1}\left(\frac{\phi_m - 1 + e^{-(Kt)^n}}{\phi_m}\right)^{[\eta]\varphi_m}. \qquad \text{(S8)}$$

This has the same form as equation (1). Dimensionally, the prefactor A in equation (1) will be proportional to η_s^{-1} multiplied by the ratio of a force (the thermodynamic driving force for needle-like crystal-growth) to a distance (representing the geometry of the film deformation process).

2.7 Fitting.

The Avrami rate-constant K was restricted to positive values, and the parameters ϕ_m and m ($=[\eta]\phi_m$) were given upper and lower bounds set by the range of values found within a variety of suspensions in the literature as follows; $0.23 < \phi_m < 0.71$, $1.31 < m < 3.77$.[24] The exponent, n, in equation S6 should, according to theory, take an integer value between 1 and 4. The Avrami model is sometimes fitted with n allowed to take non-integer values, with recent x-ray studies on annealed PCBM single layers[2] and blends[23] showing that best fits are obtained with n close to either one or two for PCBM annealed at temperatures between 150 °C and 170 °C. In our simultaneous fitting of growth-curves we fixed n to be an integer. Best fits were obtained with n set equal to one, while very good fits were also obtained with n set to two. The A and K parameters obtained from the sets of simultaneous fits with n set equal to one and two were in excellent agreement showing the robustness of the fitted values of A and K, and their dependence on PS thickness. Because, in the very earliest stages of growth the crystal can't yet be described as having developed into a high-aspect ratio needle we fitted the crystal growth-curves in two different ways. One in which we only fitted the data above a crystal length of 5μm and one in which we fitted all the collected data (down to the smallest measurable lengths of around 2μm). This would be expected to have the most significance for the shorter (sub 10μm length) needles found in the thinner PS bilayers. Within experimental error, these two approaches resulted in the same mean A and K fit parameters.

2.8 Bilayer Fabrication Scheme.

Figure S21 shows a schematic diagram of PCBM/polymer bilayer fabrication steps. To facilitate the 'floating' of the polymer film from the mica substrate, three edges of the film are gently scored with a scalpel blade, before the mica/polymer film is lowered into the de-ionized water.

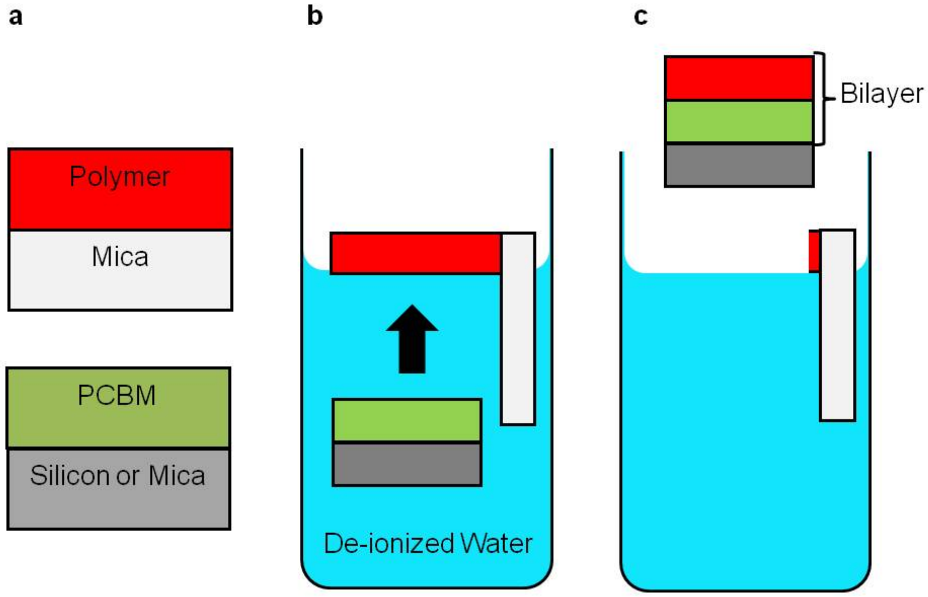

Figure S21. Schematic diagram illustrating the bilayer fabrication procedure. (a) Single layers are spin-coated onto substrates. (b) The polymer layer is 'floated' from the mica substrate onto the surface of de-ionized water. (c) The polymer layer is deposited onto the PCBM sample to make a bilayer.

References for Supplementary Information

1 Zhao, J. *et al.* Phase Diagram of P3HT/PCBM Blends and Its Implication for the Stability of Morphology. *Journal of Physical Chemistry B* **113**, 1587-1591, doi:10.1021/jp804151a (2009).

2 Verploegen, E. *et al.* Effects of Thermal Annealing Upon the Morphology of Polymer-Fullerene Blends. *Advanced Functional Materials* **20**, 3519-3529, doi:10.1002/adfm.201000975 (2010).

3 Keddie, J. L., Jones, R. A. L. & Cory, R. A. Size-Dependent Depression of the Glass Transition Temperature in Polymer Films. *Europhysics Letters* **27**, 59-64, doi:10.1209/0295-5075/27/1/011 (1994).

4 The free energy gain on crystallisation at a temperature T is given by $-\Delta H\ (T_m - T)/\ T_m$ where ΔH is the latent heat of fusion and T_m is the crystal melting point (neglecting surface terms for micron-width crystals). A melting point for pure PCBM in the range 268-288 ^{o}C (see supplementary information reference 1) results in a 10% reduction in the free energy gain between 170 ^{o}C and 180 ^{o}C.

5 Lilliu, S. *et al.* Dynamics of Crystallization and Disorder during Annealing of P3HT/PCBM Bulk Heterojunctions. *Macromolecules* **44**, 2725-2734, doi:10.1021/ma102817z (2011).

6 Zheng, L., Liu, J. & Han, Y. Polymer-regulated epitaxial crystallization of methanofullerene on mica. *Physical Chemistry Chemical Physics* **15**, 1208-1215, doi:10.1039/c2cp42614e (2013).

7 Li, L., Lu, G., Li, S., Tang, H. & Yang, X. Epitaxy-Assisted Creation of PCBM Nanocrystals and Its Application in Constructing Optimized Morphology for Bulk-Heterojunction Polymer Solar Cells. *Journal of Physical Chemistry B* **112**, 15651-15658, doi:10.1021/jp8081529 (2008).

8 Zheng, L., Liu, J., Ding, Y. & Han, Y. Morphology Evolution and Structural Transformation of Solution-Processed Methanofullerene Thin Film under Thermal Annealing. *The Journal of Physical Chemistry B* **115**, 8071-8077, doi:10.1021/jp2030279 (2011).

9 Wolff, M., Magerl, A. & Zabel, H. Structure of polymer micelles close to the solid interface. *The European Physical Journal E* **16**, 141-145, doi:10.1140/epje/e2005-00015-0 (2005).

10 Hopkinson, P. E. *et al.* A Phase Diagram of the P3HT:PCBM Organic Photovoltaic System: Implications for Device Processing and Performance. *Macromolecules* **44**, 2908-2917, doi:10.1021/ma102524a (2011).

11 Jukes, P. C. *et al.* Kinetics of Surface Crystallization in Thin Films of Poly(ethylene terephthalate). *Macromolecules* **38**, 2315-2320 (2005).

12 Avrami, M. Granulation, Phase Change and Microstructure. Kinetics of Phase Change. III. *Journal of Chemical Physics* **9**, 177-184 (1941).

13 Holzwarth, U. & Gibson, N. The Scherrer equation versus the 'Debye-Scherrer equation'. *Nature Nanotechnology* **6**, 534-534, doi:10.1038/nnano.2011.145 (2011).

14 Klug, H. P. & Alexander, L. E. *X-ray Diffraction Procedures for Polycrystalline and Amorphous Materials*. Second edn, (Wiley, 1974).

15 The reflectivity curves were measured at 80 ^{o}C to enable us to reduce the temperature jump up to the annealing temperatures of 140 ^{o}C and 170 ^{o}C. We also obtained some reflectivity curves at room temperature and found that these were the same (within experimental error) as the 80 ^{o}C measurements, confirming that nothing happens to the sample composition profile when heated at or below 80 ^{o}C.

16 Jones, R. A. L. & Richards, R. W. *Polymers at Surfaces and Interfaces*. First edn, (Cambridge University Press, 1999).

17 Sferrazza, M. *et al.* Evidence for Capillary Waves at Immiscible Polymer/Polymer Interfaces. *Physical Review Letters* **78**, 3693-3696 (1997).

18 Cubitt, R. & Fragneto, G. D17: the new reflectometer at the ILL. *Applied Physics A: Materials Science & Processing* **74**, s329-s331, doi:10.1007/s003390201611 (2002).

19 Treat, N. D. *et al.* Interdiffusion of PCBM and P3HT Reveals Miscibility in a Photovoltaically Active Blend. *Advanced Energy Materials* **1**, 82-89, doi:10.1002/aenm.201000023 (2011).

20 Higgins, J. S. & Benoit, H. C. *Polymers and Neutron Scattering*. First edn, (Oxford University Press, 1996).

21 Lee, K. H. *et al.* Morphology of All-Solution-Processed “Bilayer” Organic Solar Cells. *Advanced Materials* **23**, 766-770, doi:10.1002/adma.201003545 (2011).

22 Wong, H. C. & Cabral, J. T. Mechanism and Kinetics of Fullerene Association in Polystyrene Thin Film Mixtures. *Macromolecules* **44**, 4530-4537, doi:10.1021/ma2004458 (2011).

23 Wu, W.-R. *et al.* Competition between Fullerene Aggregation and Poly(3-hexylthiophene) Crystallization upon Annealing of Bulk Heterojunction Solar Cells. *Acs Nano* **5**, 6233-6243, doi:10.1021/nn2010816 (2011).

24 Barnes, H. A., Hutton, J. F. & Walters, K. *An Introduction to Rheology*. First edn, (Elsevier, 1989).

25 Krieger, I. M. & Dougherty, T. J. A Mechanism for Non-Newtonian Flow in Suspensions of Rigid Spheres. *Transactions of the Society of Rheology* **3**, 137-152 (1959).